

Special  
Collection

# Supercapacitive Swing Adsorption of Carbon Dioxide: Current Status and Perspectives

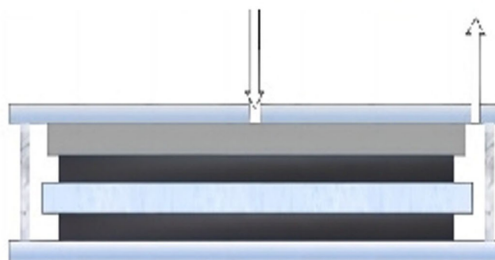
Yuanfei Wang,<sup>[a, b, c, e]</sup> Keliang Zhang,<sup>[b, c]</sup> Jijun Feng,<sup>\*[a]</sup> Xianzhong Sun,<sup>\*[b, c, d, e]</sup> Chen Li,<sup>[b, c, d, e]</sup> Kai Wang,<sup>[b, c, d, e]</sup> Xiong Zhang,<sup>[b, c, d, e]</sup> and Yanwei Ma<sup>\*[b, c, d, e]</sup>

## Electrolyte

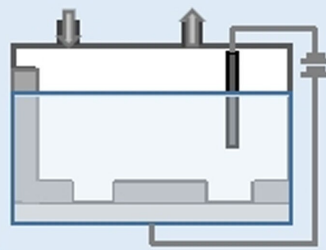


## Charge-discharge methods

### SSA module



## Carbon capture

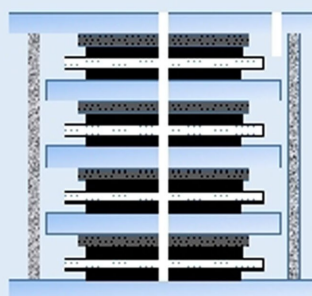


## Carbon electrode materials



## Charging protocols

## Scaling up



Supercapacitive swing adsorption (SSA) is a newly discovered electrochemically driven carbon dioxide capture method using the principle of electric double-layer capacitor, which achieves the purpose of adsorption and desorption of CO<sub>2</sub> by charging and discharging the supercapacitive electrodes. Based on this method, gas separation devices were designed which could adsorb CO<sub>2</sub> from a mixture of carbon dioxide and nitrogen, and

a series of factors affecting the CO<sub>2</sub> adsorption capacity were explored. This review briefly introduces the SSA mechanism and the structural design of SSA modules, and analyzes the factors influencing the performance of SSA from multiple aspects, with emphasis on electrode materials, in order to find ways to improve the CO<sub>2</sub> adsorption capacity of SSA modules.

## 1. Introduction

For the last 50 years, CO<sub>2</sub> in the atmosphere kept rising, and 80% of the anthropogenic CO<sub>2</sub> originated from the burning of fossil fuels.<sup>[1]</sup> In response to this problem, China has introduced policies to achieve carbon peak by 2030 and carbon neutrality by 2060.<sup>[2]</sup> At present, the main gas separation technologies in use are amine-scrubbing,<sup>[3]</sup> pressure swing adsorption (PSA),<sup>[4]</sup> vacuum swing adsorption (VSA),<sup>[5]</sup> temperature swing adsorption (TSA),<sup>[6]</sup> membrane separation techniques,<sup>[7]</sup> whereby the amine-scrubbing is the most widely used. However, aqueous amine solutions are corrosive and volatile, and the thermal desorption requires high energy consumption (60–70 kJ mol<sup>-1</sup>).<sup>[3b]</sup> PSA, VSA and TSA techniques also consume a large amount of energy due to the pressure and temperature changes.<sup>[8]</sup> Membrane separation techniques require expensive membrane materials.<sup>[9]</sup> Therefore, it is essential to seek a low-cost CO<sub>2</sub> separation technology with outstanding performance.

Supercapacitors are a class of electrochemical energy storage devices that utilize an electric double-layer formed at the interface between electrode and electrolyte to adsorb and desorb anions/cations for energy storage.<sup>[10]</sup> Typically, a supercapacitor consists of capacitive electrodes with high specific surface areas, electrolytes allowing ion migration, and sepa-

tors between electrodes.<sup>[11]</sup> In addition, rapid redox reactions occurring on the surface of electrode materials (for example, transition metal oxides or conductive polymer) have similar charge-discharge characteristics with supercapacitors, and this type of energy storage devices is also known as pseudocapacitors.<sup>[12]</sup>

In 2014, Landskron et al.<sup>[13]</sup> firstly reported the supercapacitive swing adsorption (SSA) effect, which is manifested as the reversible adsorption and desorption of CO<sub>2</sub> by charging and discharging the supercapacitive electrodes in NaCl aqueous solution. One supercapacitive electrode is partly exposed to a CO<sub>2</sub>-containing gas mixture, and the other supercapacitive electrode is completely soaked in NaCl solution. When the supercapacitor is charged, carbon dioxide is selectively adsorbed from the gas mixture, and then it is desorbed upon the supercapacitor discharged. SSA was among the earliest electrochemical concepts for carbon capture, which is far simpler than most other electrochemical techniques, and therefore more easily scalable. Compared to the redox-active and pH-swing techniques, SSA does not require changes in pressure and temperature,<sup>[15]</sup> and the low cost activated carbon materials and neutral aqueous electrolytes involved have substantial advantages in terms of capital cost. There are no corrosive or significantly toxic chemicals. In addition, supercapacitors also have a long life span (> 100,000 cycles) and have good cycling stability with a round-trip energy efficiency of > 90% for charge-discharge cycles.

[a] Y. Wang, Prof. J. Feng

School of Chemistry and Chemical Engineering

University of Jinan

Jinan 250022 (China)

E-mail: chm\_fengjj@ujn.edu.cn

Homepage: <http://chem.ujn.edu.cn/info/1030/2391.htm>

[b] Y. Wang, K. Zhang, Prof. X. Sun, Dr. C. Li, Prof. K. Wang, Prof. X. Zhang, Prof. Y. Ma

Institute of Electrical Engineering

Chinese Academy of Sciences

Beijing 100190 (China)

E-mail: xzsun@mail.iee.ac.cn

ywma@mail.iee.ac.cn

Homepage: <https://sciprofiles.com/profile/xianzhongsun>

<http://www.researchgate.net/profile/Yanwei-Ma-4>

[c] Y. Wang, K. Zhang, Prof. X. Sun, Dr. C. Li, Prof. K. Wang, Prof. X. Zhang, Prof. Y. Ma

Institute of Electrical Engineering and Advanced Electromagnetic Drive Technology

Qilu Zhongke, Jinan 250013 (China)

[d] Prof. X. Sun, Dr. C. Li, Prof. K. Wang, Prof. X. Zhang, Prof. Y. Ma

University of Chinese Academy of Sciences

Beijing 100049 (China)

[e] Y. Wang, Prof. X. Sun, Dr. C. Li, Prof. K. Wang, Prof. X. Zhang, Prof. Y. Ma

Shandong Institutes of Industrial Technology

Jinan 250102 (China)

Special Collection An invited contribution to a Special Collection on Fast Charging Batteries

### 1.1. Working mechanisms

PSA, VSA, and TSA selectively adsorb carbon dioxide onto the surface of adsorbent.<sup>[14]</sup> PSA and VSA achieve this through physical adsorption by van der Waals forces which is strongly dependent on the partial pressure of carbon dioxide.<sup>[15]</sup> TSA achieved this by adsorbing carbon dioxide either by van der Waals forces (physisorption) or through the formation of chemical bonds (chemisorption).<sup>[16]</sup>

The underlying molecular mechanisms of SSA is still insufficiently understood, which limits further improvement of SSA performances. Three possible mechanisms have been proposed to explain the SSA effect as shown in Figure 1, i.e., gas-solid adsorption mechanism, molecular liquid-solid adsorption mechanism, and ionic liquid-solid adsorption mechanism.<sup>[17]</sup> The gas-solid adsorption mechanism is thought to occur in the pores of activated carbon that are not permeated by electrolytes, next to pores that are permeated (Figure 1a). In 2018, Liu et al.<sup>[18]</sup> investigated the electrolyte

permeation behavior of BPL 4x6 (Calgon Carbon Corporation) activated carbon supercapacitor electrode by in situ neutron scattering method. The experimental results showed that only about 20% of pore volume in BPL carbon was infiltrated by 1 M NaCl aqueous electrolyte at chemical equilibrium. The infiltrated pores form electric double layer that generates capacitance. Through electron delocalization the Fermi level of neighbored,

infiltrated pores, is affected, leading to a change in adsorptivity. The second mechanism assumes that CO<sub>2</sub> molecules are adsorbed on the electric double-layer in the infiltrated pore due to the difference in CO<sub>2</sub> solubility between the electric double-layer and the bulk electrolyte (Figure 1b). The last mechanism, the ionic liquid-solid mechanism applies only to gases that can be hydrolyzed into ions. It is assumed that the gas first



Yuanfei Wang completed her B.S. study in Polymer Materials & Engineering at Jinan University in 2022. She is currently pursuing her Master's degree at University of Jinan under the supervision of Prof. Xianzhong Sun and Prof. Jijun Feng. She is one of the joint training students at the University of Jinan and Institute of Electrical Engineering, Chinese Academy of Sciences (IEE CAS). Her current research focuses on supercapacitive swing adsorption of carbon dioxide.



Keliang Zhang received his Master's degree in Materials Science & Engineering at Qilu University of Technology in 2019. He joined the Institute of Electrical Engineering, Chinese Academy of Sciences (IEE CAS) in 2021. His current research focuses on graphene-based high-performance lithium-ion capacitors. He has completed the design and development of several models of rate-type batteries, which are used in electric forklifts and sightseeing vehicles.



Prof. Jijun Feng obtained her B.S. from the Department of Applied Chemistry in Shandong Institute of building materials (1999), M.S. from School of Science and Ph. D. from School of Chemical Engineering and Technology, both in Tianjin University. Then she joined the School of Chemistry and Chemical Engineering, University of Jinan in 2004. Her current research interests are focused on the fields of novel energy storage materials for batteries, including lithium-ion batteries, sodium-ion batteries, lithium-sulfur batteries and flow batteries.



Prof. Xianzhong Sun received his Bachelor's degree from the Department of Mechanical Engineering of Wuhan Institute of Technology (1999), Master's degree from Department of Materials Science & Engineering of Zhejiang University (2006), Doctoral Degree from Department of Materials Science & Engineering of Tsinghua University (2011). He joined the Institute of Electrical Engineering, Chinese Academy of Sciences (IEE CAS) in 2011. His current research interests are in the fields of novel electrochemical energy storage devices, including electrical double-layer capacitors, lithium-ion capacitors (LIC), and lithium-ion battery type capacitors (LIBCs).



Dr. Chen Li completed his B.S. study in polymer materials and engineering at Beijing University of Chemical Technology (BUCT) in 2010 and obtained his Ph.D. degree in electrical engineering from the University of Chinese Academy of Sciences (UCAS) in 2017. In the same year, he joined the Institute of Electrical Engineering (IEE), Chinese Academy of Sciences (CAS). His research interests focus on the design and fabrication of advanced carbon-based energy materials for high-performance supercapacitors and lithium-ion capacitors.



Prof. Kai Wang received his B.S. degree from the Department of Chemistry and Chemical Engineering of Shandong University (2007), and his Ph.D. degree from the National Center for Nanoscience and Technology (NCNST). After a postdoctoral experience in Singapore-MIT Alliance for Research and Technology (SMART), he joined the Institute of Electrical Engineering, Chinese Academy of Science in 2014. His current research interests are in the field of electrochemical energy materials and devices, with a focus on hybrid nanomaterials, supercapacitors, and solid-state lithium-ion batteries.



Prof. Xiong Zhang received his B.S. degree in applied chemistry from Central South University in 2003, and his Ph.D. in applied chemistry from Beijing University of Chemical Technology in 2008. Then he joined the Institute of Electrical Engineering, Chinese Academy of Sciences. His research interests focus on the synthesis of electrode materials for supercapacitors and the applications of lithium-ion capacitors.



Prof. Yanwei Ma obtained his Ph.D. degree from Tsinghua University in 1996 and then worked as a post-doctoral fellow at the University of Science and Technology Beijing (USTB). Following research associate positions at Institute for Materials Research, Tohoku University (Sendai, Japan), National Institute for Materials Science (Tsukuba, Japan), and Université de Rennes 1 (France), he joined the Institute of Electrical Engineering, Chinese Academy of Sciences in 2004 as a full-time professor. He leads a team focused on superconductivity and new energy materials. His research activities are devoted to the development of superconducting wires and nanomaterials for energy storage, and fabrication of graphene-based supercapacitors.

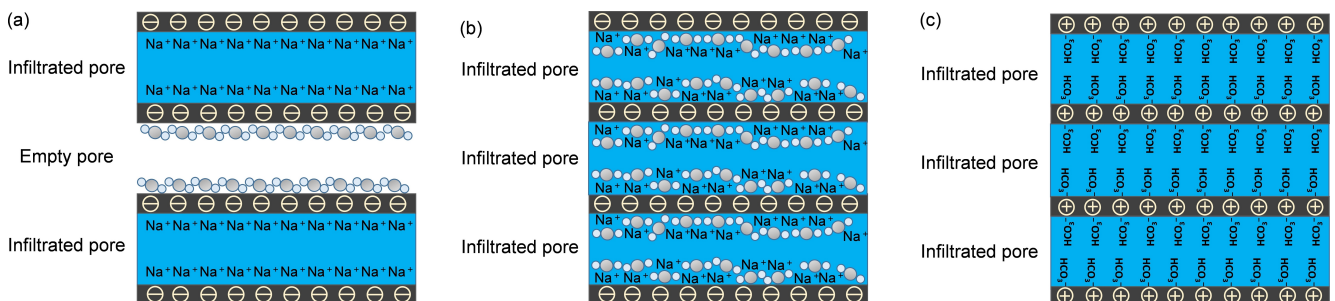


**Figure 1.** a) Gas-solid mechanism (illustrated for the adsorption at the negative electrode), b) molecular liquid-solid mechanism (illustrated for the adsorption at the negative electrode), c) ionic liquid-solid mechanism. Reproduced from ref. [21] Copyright (2019), with permission from American Chemical Society.

hydrolyzes to form ions, and then the ions are adsorbed to the electrodes via electrostatic forces. In a carbon capture applications, carbon dioxide gas is hydrolyzed to form bicarbonate, and the supercapacitive positive electrode adsorbs bicarbonate anions (Figure 1c).<sup>[19]</sup> In addition, proton adsorption to the negative electrode can lead to a pH increase in the bulk solution, and thus to adsorption of CO<sub>2</sub> into the bulk electrolyte.<sup>[20]</sup> Nevertheless, there is no consensus on the important scientific issue of the SSA mechanism of carbon dioxide, and the quantitative analysis of these mechanisms remains to be studied.

## 1.2. Device design

The design of SSA module has roughly gone through three stages. In 2014, a prototype gas adsorption cell was designed to demonstrate the supercapacitive swing adsorption effect. The gas adsorption cell had monolithic, cylindrical carbon electrodes and an aqueous solution electrolyte (1 M NaCl), as shown in Figure 2(a), which can selectively and reversibly adsorb CO<sub>2</sub> from a 15% CO<sub>2</sub>/85% N<sub>2</sub> gas mixture, and adsorption and desorption of carbon dioxide occurs when charging and discharging the supercapacitor. The pressure changes were observed during galvanostatic charging and discharging (GCD), and the pressure versus time curves are illustrated in Figure 3.<sup>[13]</sup> However, this gas adsorption cell was not suitable for separating gas from continuous gas streams. In 2017, Liu et al.<sup>[22]</sup> designed a SSA module that can separate CO<sub>2</sub> from a

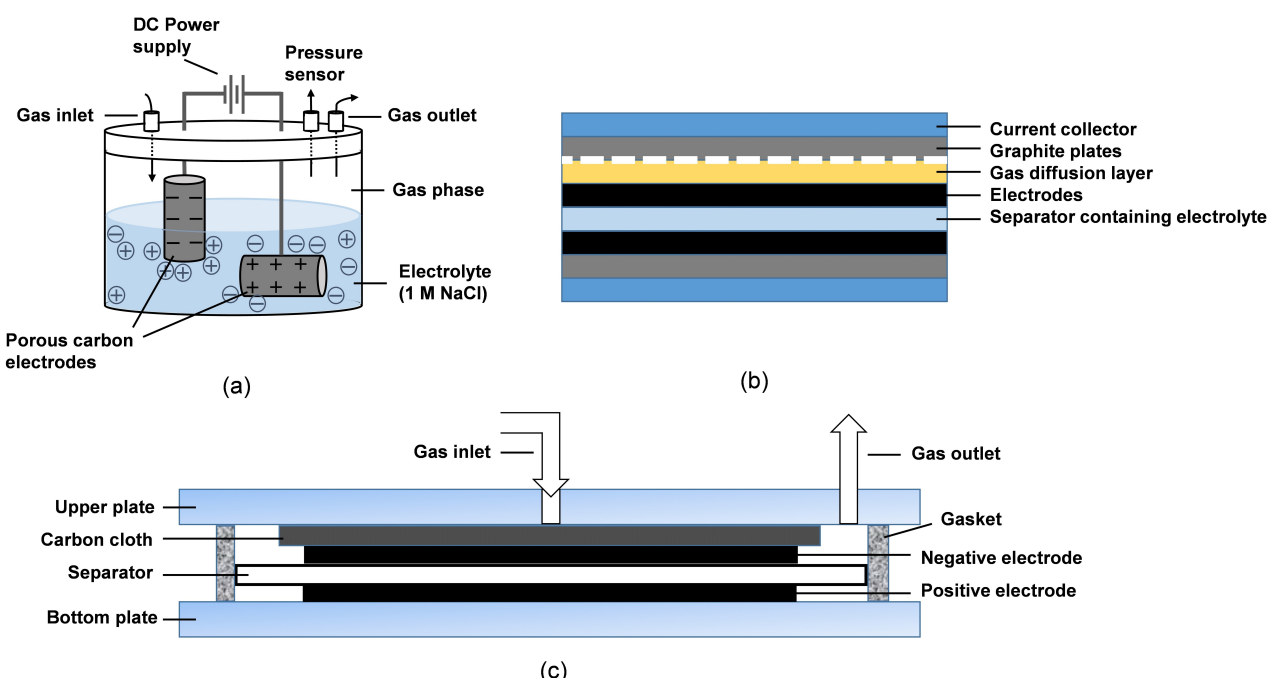


**Figure 2.** a) Prototype device to study the effects of SSA with aqueous electrolytes, with the negative electrode is partially immersed in the electrolyte, the positive electrode is fully immersed. Reproduced from ref. [13] Copyright (2014), with permission from Wiley-VCH. b) SSA module with a coin-type structure. Reproduced from ref. [22] Copyright (2017), with permission from The Royal Society of Chemistry. c) SSA gas separation module for radial gas flows, cross-sectional view. Reproduced from ref. [17] Copyright (2018), with permission from American Chemical Society.

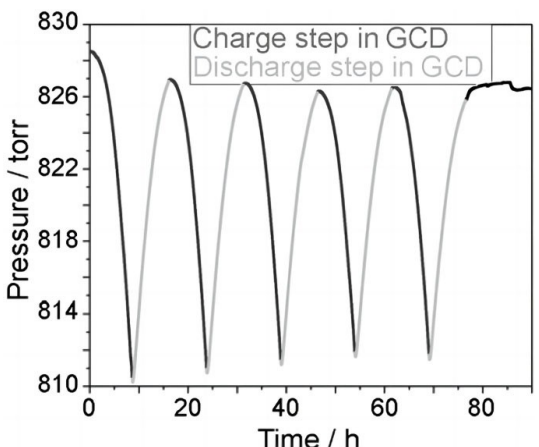


**Figure 3.** Pressure changes observed during galvanostatic charging and discharging processes. Reproduced from ref. [13] Copyright (2014), with permission from Wiley-VCH.

gas stream, which contains elements of coin type supercapacitors and fuel cells. Its major constituents are a separator (filter paper) soaked with an aqueous electrolyte, and carbon cloth diffusion layers as shown in Figure 2(b). Compared with the original prototype module, it has lower internal resistance and faster gas diffusion kinetics. In 2018, Zhu et al.<sup>[17]</sup> expanded and simplified the original module, designed a novel SSA module for radial gas flows as shown in Figure 2(c), and defined the energy and adsorption metrics of SSA. With the continuous improvement of the modules, their energy consumption (EC) and adsorption capacity (AC) for CO<sub>2</sub> were also continuously improving, among which the initial SSA module designed in 2017 has the lowest energy consumption of 57 kJ mol<sup>-1</sup>, while the enlarged and simplified SSA module in 2018 has the highest CO<sub>2</sub> adsorption capacity of 63 mmol kg<sup>-1</sup>,<sup>[17]</sup> as shown in Figure 4.

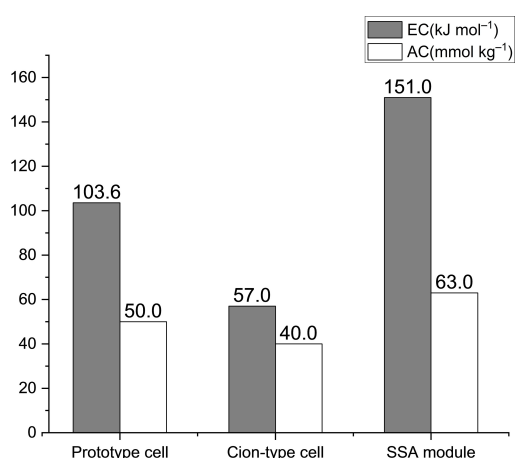


**Figure 4.** Energy consumption and CO<sub>2</sub> adsorption capacity of the three structural design from 2014 to 2018.

## 2. Factors Influencing SSA Performances

Compared with the conventional amine-scrubbing method [adsorption capacity (AC): 800 mmol kg<sup>-1</sup>], the AC of the supercapacitive swing adsorption of CO<sub>2</sub> was low (typical value 60 mmol kg<sup>-1</sup> based on the weight of activated carbon in the gas exposed electrode), for which the influencing factors of the adsorption performance are urgently required. Since 2014, the researchers focused on the improvement of the CO<sub>2</sub> adsorption capacity by optimizing the components and the device design, e.g., electrolyte, electrode materials, charge-discharge methods. The further improvement and the achievement of the optimal AC in SSA will be the key subject of the future research.

### 2.1. Charge-discharge methods

The influence of charge-discharge methods on SSA performance were explored in three aspects: charging current, holding steps and holding step length, including four charge-discharge protocols, i.e., "GCD", "GCD + Pstat", "GCD + OC", and "Combined". "GCD" stands for galvanostatic charge-discharge method. "GCD + Pstat" protocol represents the GCD processes with additional 30-min potentiostatic holding steps after each charging and discharging. "GCD + OC" represents the GCD processes with additional 30-min open-circuit holding steps after each charging and discharging. "Combined" protocol represents the GCD processes with an additional open-circuit holding step.<sup>[17]</sup>

It was reported that the galvanostatic charging and discharging at 50 mA has the adsorption rate (33 μmol kg<sup>-1</sup> s<sup>-1</sup>) and time energy efficiency (8.1 μmol kJ<sup>-1</sup> s<sup>-1</sup>).<sup>[17]</sup> However, except for a constant current of 10 mA (GCD10), the CO<sub>2</sub> concentration after discharged at the current of 20 mA (GCD20), 50 mA (GCD50) and 100 mA (GCD100) is less than 15%, which indicates that rapid charging and discharging can lead to a large degree of adsorption and desorption kinetic lag (Figure 5), hence there are limits with regards to how much one can increase adsorption rates by increasing charge rates. It was observed that the decrease of CO<sub>2</sub> adsorption capacity is larger than the specific capacitance, which indicates that the decrease of adsorption capacity is not only correlated to the capacitance, but more importantly, the high charge-discharge rate leads to an increase in the lag of adsorption and desorption. Therefore, it was considered to add a hold step after each GCD process in order to compensate for the shortcoming of this approach.

For the "GCD", "GCD + Pstat", "GCD + OC", and "Combined" experiments in Ref. [17], the constant current was 50 mA, since GCD50 possessed excellent adsorption properties and relatively short cycle times as shown in Figure 6(a). The holding step length was 30 min, within which it is enough to achieve CO<sub>2</sub> adsorption thermodynamic equilibrium. The "Combination" protocol had the lowest energy consumption (151 kJ mol<sup>-1</sup>) and the highest adsorption capacity (63 mmol kg<sup>-1</sup>) as shown in Figure 6(b).

Therefore, introducing a holding step greatly enhances the CO<sub>2</sub> adsorption capacity, as it allows the completion of gas

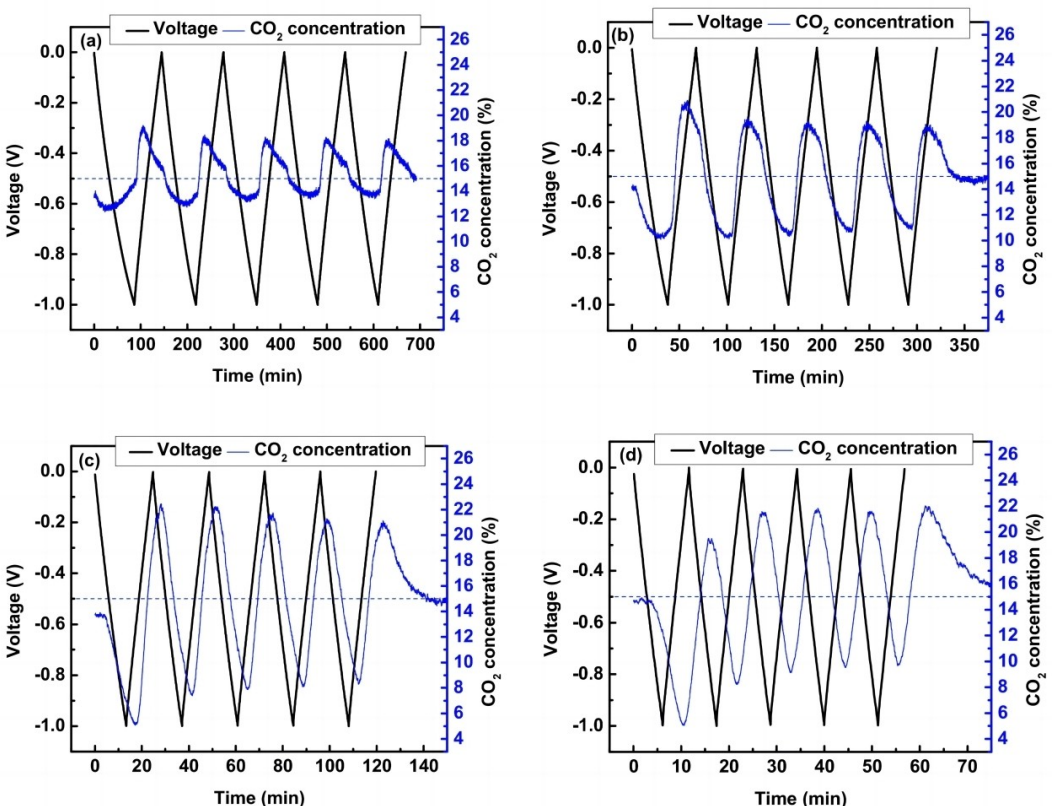


**Figure 5.** The voltage response and  $\text{CO}_2$  concentration obtained by GCD testing of SSA modules at different constant currents. a) GCD10 (charged at 10 mA), b) GCD20 (charged at 20 mA), c) GCD50 (charged at 50 mA), and d) GCD100 (charged at 100 mA). Reproduced from ref. [17] Copyright (2018), with permission from American Chemical Society.

adsorption with kinetic lag behind the charge-discharge process. Nevertheless, on account of the self-discharge during the holding step, energy loss will increase.

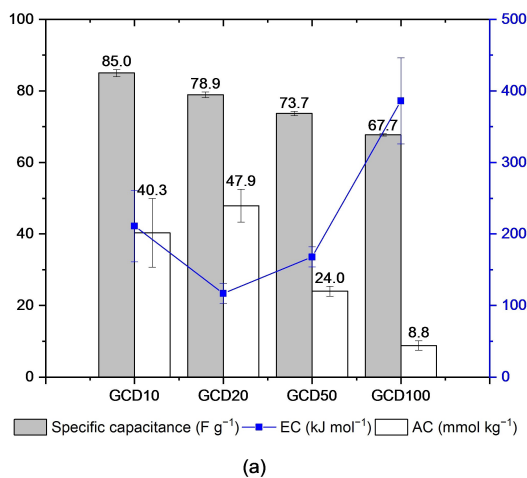
## 2.2. Electrolyte

### 2.2.1. Concentration

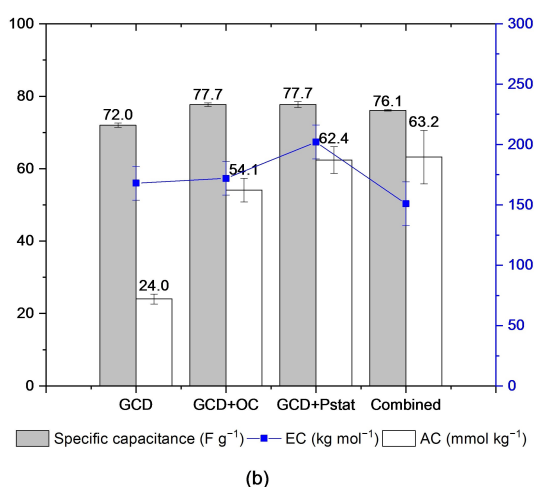
At present, the most commonly used electrolyte for the supercapacitive swing adsorption of  $\text{CO}_2$  is 1 M NaCl aqueous solution.<sup>[21]</sup> It can be seen that the adsorption capacity of  $\text{CO}_2$  will increase with the increase of the concentration of NaCl solution between 0–1 M, while the adsorption capacity ( $62\text{--}63 \text{ mmol kg}^{-1}$ ) will remain almost unchanged after 1 M, which also explains the rationality of choosing 1 M NaCl as the electrolyte for most experiments. In addition, Zhu et al.<sup>[21]</sup> found that higher concentrations of NaCl aqueous electrolytes lead to lower resistance and energy consumption at 0–5 M, except for 5 M NaCl because the internal resistance was slightly higher than 3 M NaCl, as shown in Figure 7, which was attributed to the strong solvation effects and/or local NaCl crystallization in electrode pores.

### 2.2.2. Elemental composition

Recently, Zhu et al.<sup>[19]</sup> investigated the influence of electrolyte cation and electrolyte anion on SSA performance. It was found that the resistance sequences of capacitors with different electrolyte elements coincided with the order of their ion mobility, indicating that the liquid phase ion resistance plays a decisive role in the SSA internal resistance. Notably, the conductivity of  $\text{NaHCO}_3$  solution is more consistent with that of  $\text{CO}_3^{2-}$  ions, suggesting that the  $\text{CO}_3^{2-}$  anion in equilibrium with  $\text{HCO}_3^-$  determines the overall conductivity. Additionally, the specific capacitance increases with the rising ionic potential due to the higher charge density of ions can better compensate for the opposite charge accumulated on the electrode surface, where the cation and anion electrolytes with the highest specific capacitance are  $\text{MgCl}_2$  ( $82.0 \text{ F g}^{-1}$ ) and  $\text{NaBr}$  ( $91.4 \text{ F g}^{-1}$ ), respectively, while  $\text{MgCl}_2$  ( $129 \text{ kJ mol}^{-1}$ ) and  $\text{NaBr}$  ( $125 \text{ kJ mol}^{-1}$ ) also have the lowest energy consumption as shown in Figure 8. Furthermore, it was noticed that the performance of individual ions could be increased synergistically. Taking  $\text{MgBr}_2$  as an example, the highest  $\text{CO}_2$  adsorption capacity of  $67.3 \text{ mmol kg}^{-1}$  and the lowest energy consumption of  $90 \text{ kJ mol}^{-1}$  were obtained by the “GCD + Pstat” method, which is superior to the results obtained by the previous mentioned cations or anions only.



(a)



(b)

**Figure 6.** Performance metrics of SSA modules. a) “GCD” method at different currents, b) GCD method with different holding steps. Reproduced from ref. [17] Copyright (2018), with permission from American Chemical Society

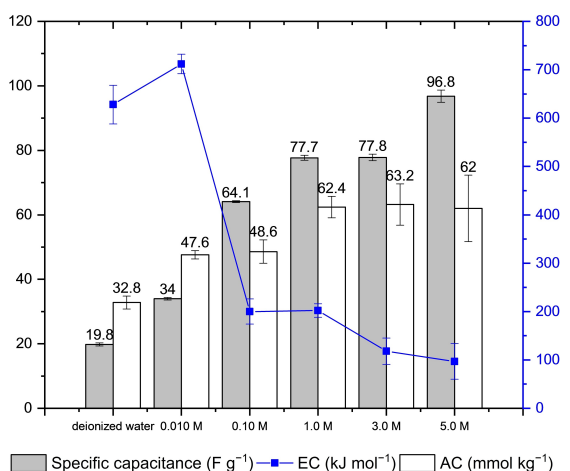


**Figure 7.** Performance metrics of SSA modules using NaCl solution of different concentration as the electrolyte. Reproduced from ref. [21] Copyright (2019), with permission from American Chemical Society

In general, the performance of SSA is not much dependent on the nature of the ions in the electrolyte, so Zhu and co-

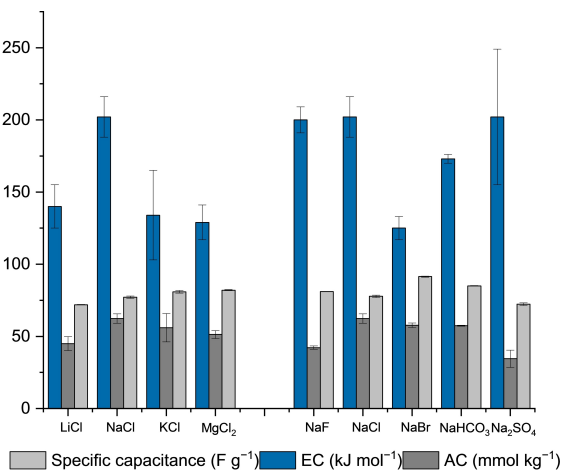


**Figure 8.** Performance metrics of the SSA modules for different elemental composition of electrolytes. Reproduced from ref. [19] Copyright (2018), with permission from American Chemical Society

workers<sup>[19]</sup> used seawater (from North Carolina) as the electrolyte in the SSA module and found that seawater exhibited comparable internal resistance, specific capacitance, coulombic efficiency, energy efficiency and energy loss compared to the above experimental results, but it had a lower CO<sub>2</sub> sorption capacity (31.9 mmol kg<sup>-1</sup>) due to the lower salt concentration (about 0.5 M). It implies that seawater can be used as an electrolyte for SSA modules, and in the future SSA may be used to capture CO<sub>2</sub> from seawater to reduce ocean acidification.

### 2.3. Carbon electrode materials

The electrode materials for SSA cells include porous carbon from various sources, such as biomass,<sup>[23]</sup> coal,<sup>[24]</sup> carbide<sup>[25]</sup> and coke.<sup>[26]</sup> The porous structure of these materials can enhance the electric double-layer capacitance, thereby boosting the CO<sub>2</sub> gas adsorption performances. There is literature available that examines the performance of carbon electrode materials with the potential to increase specific capacitance. This review summarizes these findings with the aim of applying them to future SSA modules.<sup>[27]</sup>

#### 2.3.1. Fossil fuel-derived activated carbon

Activated carbon-based electrode materials show great potential for the supercapacitive swing adsorption of CO<sub>2</sub> due to their high porosity and large specific surface area.<sup>[28]</sup> One of the important sources of raw materials for traditional activated carbon is fossil fuel, which offers the advantages of mature technology and high yield, but also has the limitations of low capacitance and non-renewable precursors.<sup>[29]</sup> In a recent study by Bilal et al.,<sup>[23]</sup> commercially available carbon from three different raw materials (coal, carbide, and coke) was used for CO<sub>2</sub> adsorption: Coal-derived BPL 4x6 carbon (Calgon), carbide-derived Y carbon (Y-Carbon) and coke-derived Supersorb

carbon (Amoco Carbon). Among them,  $4\text{ cm}^2$  electrodes prepared from Supersorb activated carbon showed the highest  $\text{CO}_2$  adsorption capacity ( $201\text{ mmol kg}^{-1}$ ) and the lowest energy consumption ( $204\text{ kJ mol}^{-1}$ ) at  $50\text{ mA g}^{-1}$  as shown in Figure 9. BPL carbon, as a fossil fuel derived carbon, has the poorest performance of the three activated carbons. However, fossil fuel-derived activated carbon has the most abundant source and lowest raw material cost, which holds the potential to further improve its performance, e.g., in terms of higher specific capacitance and  $\text{CO}_2$  adsorption capacity. All of these factors are beneficial for large-scale  $\text{CO}_2$  capture.

### 2.3.2. Biomass-derived activated carbon

Biomass-derived activated carbons have shown promising prospects for high-performance energy storage, gas adsorption, and water treatment applications, thanks to their advantages of

abundant resources and low-cost production.<sup>[30]</sup> The garlic root from the Music type Hardneck garlic (K.V. farm, Stroudsburg, Pennsylvania), garlic powder (Badia spices, Doral, Florida) and garlic skin (Spice World) have been comparatively investigated as raw materials for activated carbons.<sup>[23]</sup> Among them, garlic root-derived activated carbon has the highest capacitance performance ( $257\text{ F g}^{-1}$ ) and  $\text{CO}_2$  adsorption performance ( $273\text{ mmol kg}^{-1}$ ), and the energy consumption of garlic root and garlic powder-derived activated carbon ( $177\text{--}179\text{ kJ mol}^{-1}$ ) is lower than that of previously mentioned BPL activated carbon as shown in Figure 10. This review summarizes biomass-derived activated carbons with high specific capacitance and/or high specific surface area, including rice husks, orange peels, and peanut shells, etc. The relevant information of the activated carbons are listed in Table 1. As mentioned earlier, SSA performance is significantly related to the specific surface area and specific capacitance of activated carbon. And thus, these data can provide options for screening suitable carbon materials, and thereby facilitating more efficient exploration of high SSA performances of biomass-derived activated carbon in the future.

### 2.3.3. Heteroatom doped carbon electrode materials

The introduction of doping atoms in certain biomass sources has shown to enhance the electrochemical performances of electrode materials.<sup>[50]</sup> Since activated carbon-based electrode materials in supercapacitors have a limited capacitance stored only through the electric double-layer. However, the introduction of heteroatoms (e.g., N, S, P) into activated carbons can modify their surface structure and result in enhanced electrochemical performance. The merits of heteroatom doping can be summarized as follows: (1) change the internal electronic structure of activated carbon by changing the Fermi energy level, thus enhancing its electrical conductivity;<sup>[51]</sup> (2) improve the wettability and pore utilization rate of activated carbon in electrolyte by change the surface pole of activated carbon;<sup>[52]</sup> (3) heteroatoms incorporated into the carbon backbone, leading to more structural defects and provide more active sites.

Nitrogen atoms easily replace the carbon atoms in the lattice structure of the carbon backbone due to their similar atomic radius.<sup>[53]</sup> The additional solitary pair of electrons provided by nitrogen doping contributes to the delocalized  $\pi$  bonds in the carbon skeleton, improving the conductivity and hydrophilicity of the carbon materials, and enhancing the interaction with electrolyte ions.<sup>[54]</sup> Wang et al.<sup>[55]</sup> prepared nitrogen-doped activated carbon using poly-p-phenylenediamine as raw material combined with reduced graphene oxide (rGO), and its nitrogen content was about 7.91 wt%, with a large specific capacity of  $158.5\text{ F g}^{-1}$  at the current density of  $1\text{ A g}^{-1}$  in 6 M KOH aqueous electrolytes.

Boron, which is located before carbon in the periodic table, has a similar atomic radius to carbon and one less electron number than carbon, making it another ideal heteroatom. The valence electron structure of boron is  $2\text{ s}^2\text{ p}^1$ , which provides

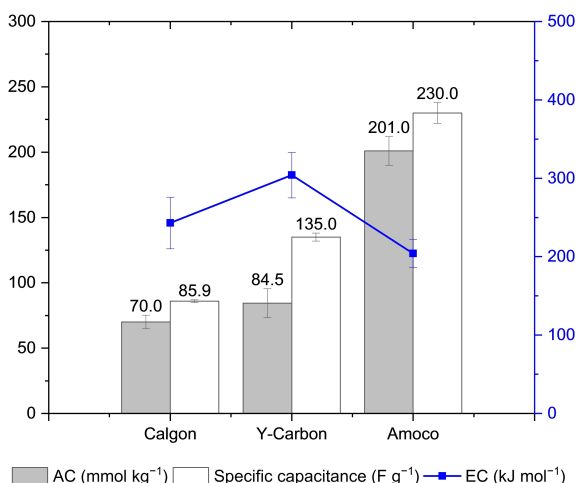


**Figure 9.** Performance Metrics of different fossil fuel-derived activated carbon. Reproduced from ref. [23] Copyright (2022), with permission from ChemRxiv.

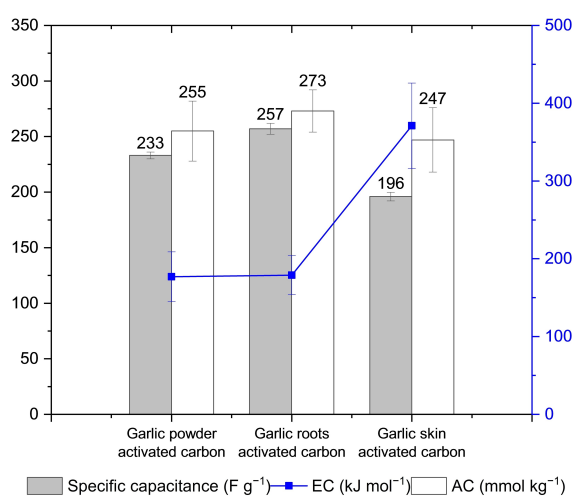


**Figure 10.** Performance Metrics of garlic powder, root, stem derived activated carbon electrodes. Reproduced from ref. [23] Copyright (2022), with permission from ChemRxiv.

**Table 1.** Comparison of various biowaste derived activated carbons.

Source	Activation method	Surface area [m <sup>2</sup> g <sup>-1</sup> ]	Specific capacitance [Fg <sup>-1</sup> ]	Electrolyte	Ref.
Rice husk	KOH	3145	367 at 5 mVs <sup>-1</sup>	6 M KOH	[31]
Orange peel	KOH	2160	460 at 1 Ag <sup>-1</sup>	1 M H <sub>2</sub> SO <sub>4</sub>	[32]
Pomelo peel	KOH	832	374 at 0.1 Ag <sup>-1</sup>	6 M KOH	[33]
Peanut shell	ZnCl <sub>2</sub>	1549	340 at 1 Ag <sup>-1</sup>	1 M H <sub>2</sub> SO <sub>4</sub>	[34]
Baobab fruit shell	H <sub>3</sub> PO <sub>4</sub>	2135	356 at 1 Ag <sup>-1</sup>	4 M KOH	[35]
Renewable corn straw and soy protein	KOH	1413	379 at 0.05 Ag <sup>-1</sup>	6 M KOH	[36]
Tobacco stalks	KOH	3733	423 at 1 Ag <sup>-1</sup>	6 M KOH	[37]
Coffee bean	ZnCl <sub>2</sub>	1019	368 at 5 Ag <sup>-1</sup>	1 M H <sub>2</sub> SO <sub>4</sub>	[38]
Yerba mate	KOH	1800	644 at 0.1 Ag <sup>-1</sup>	1 M KOH	[39]
Tea leaves	KOH	2841	330 at 1 Ag <sup>-1</sup>	2 M KOH	[40]
Ginkgo leaves	KOH	2948	323 at 0.5 Ag <sup>-1</sup>	6 M KOH	[41]
Aloe vera	KOH	1890	410 at 0.5 Ag <sup>-1</sup>	1 M H <sub>2</sub> SO <sub>4</sub>	[42]
Soybeans pods	NaOH	2612	353 at 0.5 Ag <sup>-1</sup>	1 M Na <sub>2</sub> SO <sub>4</sub>	[43]
Cooked chicken bone	KOH	2235	329 at 1 Ag <sup>-1</sup>	1 M NaNO <sub>3</sub>	[44]
Mangosteen peels	NaOH	2623	357 at 1 Ag <sup>-1</sup>	6 M KOH	[45]
Stems of Prosopis juliflora	KOH	315	307 at 0.5 Ag <sup>-1</sup>	1 M H <sub>2</sub> SO <sub>4</sub>	[27b]
Daylily	KOH	1531	299 at 0.5 Ag <sup>-1</sup>	6 M KOH	[46]
Willow wood	KOH	2800	294 at 1 Ag <sup>-1</sup>	6 M KOH	[47]
Cherry flower	KOH	2025	334 at 0.5 Ag <sup>-1</sup>	6 M KOH	[48]
Nelumbo nucifera (Lotus) seed	KOH	2330	379 at 1 Ag <sup>-1</sup>	1 M H <sub>2</sub> SO <sub>4</sub>	[49]

three electrons and an empty orbital. This change in the electronic structure influences the electric double-layer capacitance of carbon materials.<sup>[56]</sup> Low concentration boron doping is particularly significant as it enhances the redox reaction of oxygen-containing functional groups, thereby resulting in an increase in pseudocapacitance.<sup>[57]</sup> Devarajan et al.<sup>[27b]</sup> synthesized boron-doped active biomass-derived carbon from the stem of *Prosopis juliflora*, which has a higher specific capacitance of 307 Fg<sup>-1</sup> at the current density of 0.5 Ag<sup>-1</sup>.

Binding sulfur into the carbon chain is more challenging, and it typically exists in carbon materials in the form of thiophene sulfur, sulfoxide, sulfon and sulfonic acid,<sup>[58]</sup> which increases the charge density on the surface of carbon atoms, and facilitates charge transfer. Sulfoxide and sulfone can participate in redox reactions to produce certain pseudocapacitance. In addition, sulfur often interacts synergistically with other heteroatoms further enhancing the electrochemical performances of the carbon materials. He et al.<sup>[59]</sup> prepared a sulfur-doped activated carbon by 5.54 at% sulfur doping at 700 °C. The resulting material exhibited a high specific capacitance of 207 Fg<sup>-1</sup> at the current density of 1 Ag<sup>-1</sup>, compared to the sample without sulfur doping (116 Fg<sup>-1</sup> at 1 Ag<sup>-1</sup>).

Incorporating phosphorus into the carbon backbone is challenging as it tends to form bonds with C or O.<sup>[60]</sup> However, phosphorus atoms have a high electron-giving ability that can significantly enhance the charge storage and transport capability of activated carbon. Sun et al.<sup>[61]</sup> synthesized phosphorus-modified onion-like carbon using triphenylphosphine as phosphorus source, and found that the formation of C—O—P

bonds increased the activity of oxygen reduction reaction (ORR), while C—P bonds led to reduced reactivity. Natural phosphorus doping in biomass can yield structures superior to artificial doping. Lei et al.<sup>[62]</sup> prepared carbon material with a phosphorus content of 1.46 at% using the precursor of *Pulsatilla chinensis* (Bunge) Regel. The phosphorus-doped material obtained from the phosphorus-containing plants exhibited excellent oxygen reduction performance, providing a promising avenue for increasing the pseudocapacitance.

#### 2.3.4. Other carbon based composites

Commonly, the carbon based composite materials for supercapacitors consist of transition metal oxide and Nanostructured carbon materials, e.g., graphene, carbon nanotubes, carbon aerogels.<sup>[27d,29]</sup>

Graphene, a single layer two dimensional honeycomb lattice structure, has a large specific surface area, excellent mechanical flexibility, outstanding electrical performance and a high theoretical capacitance ~550 Fg<sup>-1</sup>.<sup>[63]</sup> However, graphene nanolayers tends to reaccumulate due to limited interlayer spacing.<sup>[64]</sup> Therefore, MnO<sub>2</sub>/graphene composites are synthesized to prevent the agglomeration of graphene by introducing MnO<sub>2</sub> particles between the layers.<sup>[29]</sup> Zhang et al.<sup>[65]</sup> prepared an asymmetric supercapacitor composed of a graphene foam/MnO<sub>2</sub> electrode and a graphene foam/polypyrrole electrode, and their specific capacitance were 548.6 and 434.2 Fg<sup>-1</sup> at 1 mA cm<sup>-2</sup>, respectively, which was a significant advancement

compared to the specific capacitance of  $135 \text{ F g}^{-1}$  reported by Stoller et al. in 2008 for the first graphene-based supercapacitor.<sup>[66]</sup>

Carbon nanotubes (CNT), hollow tubes formed by rolling up single layer graphene (SWNT) or multilayer graphene (MWNT), possess exceptional mechanical, electrical and thermal performances.<sup>[67]</sup> It is aimed to enhance the specific capacitance of CNTs by incorporating  $\text{MnO}_2$  with high pseudocapacitance.<sup>[68]</sup> Pecenek et al.<sup>[69]</sup> prepared a  $\text{NiO}/\text{MnO}_2/\text{carbon CNT}$  composite, which obtained a large specific capacitance of  $1320 \text{ F g}^{-1}$  at  $1 \text{ A g}^{-1}$ .

Carbon aerogels are special low-density microcellular foams with high specific surface area and conductivity.<sup>[70]</sup> To date, several researchers have made remarkable progress in enhancing the specific capacitance of carbon aerogels through the integration of  $\text{MnO}_2$  with carbon aerogels.<sup>[71]</sup> Lai et al.<sup>[71b]</sup> developed PAN/polyimide carbon aerogels with  $\text{MnO}_2$  and utilized them in supercapacitors, resulting in a maximum capacitance of  $1066 \text{ F g}^{-1}$ .

The specific capacitance of carbon electrodes basically shows a positive correlation with  $\text{CO}_2$  adsorption capacity. Therefore, it can be expected that the optimization of the capacitive properties of graphene, carbon nanotubes, and carbon aerogels will be of great help in the future exploration of carbon electrodes with high  $\text{CO}_2$  adsorption capacity.

#### 2.4. Charging protocols

Generally, the SSA electrochemical cell is negatively charged with the negative electrode partly exposed to the  $\text{CO}_2$  gas, which is termed as "negative charging", i.e.,  $\text{CO}_2$  is adsorbed when the cell voltage decreases from  $0 \text{ V}$  to  $-1 \text{ V}$ ; the adsorbed  $\text{CO}_2$  is released when the cell voltage returns to  $0 \text{ V}$ .<sup>[20]</sup> The SSA electrochemical cell can also be positively charged from  $0 \text{ V}$  to  $+1 \text{ V}$  with the working electrode partly exposed to the  $\text{CO}_2$  gas, termed as "positive charging", and the adsorbed  $\text{CO}_2$  gas is released upon charging. It could be concluded that, regardless of negative or positive voltage, lowering the cell voltage always leads to  $\text{CO}_2$  adsorption, while increasing the voltage always leads to desorption. Therefore, Binford et al.<sup>[20]</sup> improved the adsorption capacity by combining the positive charging and

negative charging protocols into a "switching" protocol, expanded the cell voltage range with  $-1 \text{ V}$  and  $+1 \text{ V}$  as voltage limits. This results in a higher adsorption capacity ( $112 \text{ mmol kg}^{-1}$ ), which is significantly larger than the adsorption capacity of the traditional negative charging protocol ( $50 \text{ mmol kg}^{-1}$ ) and the positive charging protocol ( $75 \text{ mmol kg}^{-1}$ ), as shown in Figure 11. However, the limitations of this new method are increased energy consumption ( $751 \text{ kJ mol}^{-1}$ ) and irreversible pressure drops, indicating the need for further optimization of equipment and materials for practice.

In addition, it was found that appropriately increasing the charging voltage can increase the  $\text{CO}_2$  adsorption capacity, but this will increase energy consumption, and excessive charging voltage will reduce capacitance performance. Li et al.<sup>[72]</sup> employed the garlic roots activated carbon electrode, expanding the negative charging voltage from  $-1.0 \text{ V}$  to  $-1.4 \text{ V}$ , the energy consumption increased only slightly ( $130 \text{ kJ mol}^{-1}$ ), and a high  $\text{CO}_2$  adsorption capacity of  $461 \text{ mmol kg}^{-1}$  was achieved, which was greatly improved compared with the  $\text{CO}_2$  adsorption capacity ( $312 \text{ kJ mol}^{-1}$ ) obtained from  $-1.0 \text{ V}$  negative charging, in addition to the high specific capacitance and stable SSA performances of the garlic roots activated carbon as shown in Figure 12(a). In the experiment with a gas flow rate of  $5 \text{ sccm}$  (standard cubic centimeter per minute), and a charging voltage from  $0$  to  $-1.4 \text{ V}$  a higher  $\text{CO}_2$  adsorption capacity of  $524 \text{ mmol kg}^{-1}$  was obtained as shown in Figure 12(b). However, by increasing the charging voltage to  $1.6 \text{ V}$  and above, significant deviations from the capacitive behavior due to redox processes were observed, and the energy consumption was significantly higher.

#### 2.5. Scaling up

Bilal et al.<sup>[23]</sup> found that directly expanding the electrode area slightly reduces the adsorption performance of the SSA module. Recently, they scaled SSA modules by connecting bipolar electrode pairs in series for 2, 4, 8, 12 pairs stacks, applying corresponding final voltages ( $2 \text{ V}$ ,  $4 \text{ V}$ ,  $8 \text{ V}$  and  $12 \text{ V}$ ) and flow rates ( $6 \text{ sccm}$ ,  $16 \text{ sccm}$ ,  $24 \text{ sccm}$  and  $36 \text{ sccm}$ ) to them, respectively.<sup>[73]</sup> It is noticed that the absolute adsorption

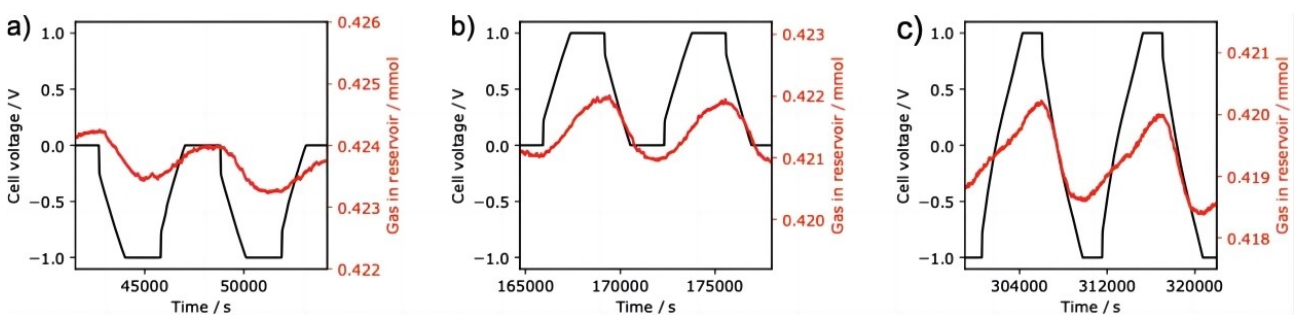
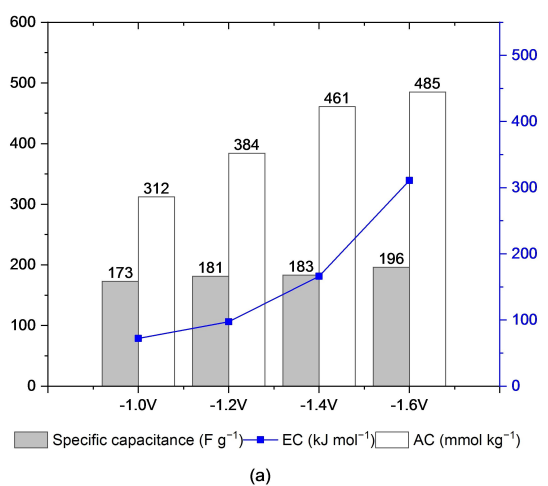
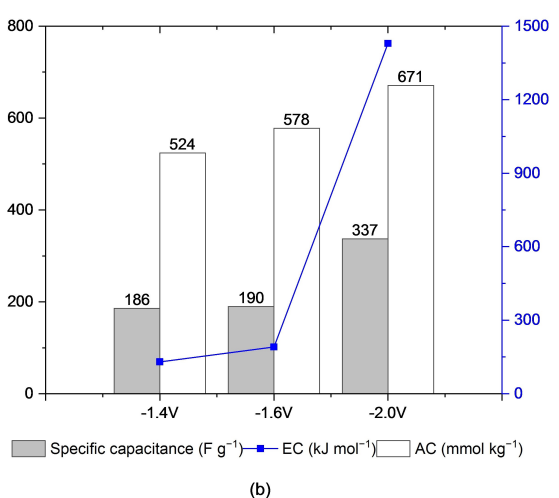


**Figure 11.** Gas adsorption curves: a) negative charging, b) positive charging, c) both negative charging and positive charging, as well as changing the applied voltage between positive and negative. Cell voltage is between the gas-exposed electrode and the counter electrodes conducted with  $1 \text{ M NaCl}$  electrolyte,  $15 \text{ mg}$  electrodes,  $30 \text{ mAg}^{-1}$  current density, and at a temperature of  $30^\circ\text{C}$ . Reproduced from Ref. [20] Copyright (2022), with permission from Royal Society of Chemistry.



(a)



(b)

**Figure 12.** a) Performance metrics of garlic roots activated carbon electrode under different potential windows, b) performance metrics of SSA at higher voltage window and 5 sccm flow-rate. Reproduced from Ref. [72] Copyright (2023), with permission from Small.

capacity and productivity of  $\text{CO}_2$  in the module increase proportionally with the increase in the number of electrode pairs, i.e., from 151 to 787  $\mu\text{mol}$ , and from 70 to 390  $\text{mmol h}^{-1} \text{m}^{-2}$ , respectively, and that the increase in electrode pairs reduces energy consumption, i.e., from 202 to 60  $\text{kJ mol}^{-1}$ . The scalability was demonstrated across all stacks, with the adsorption capacity ( $\sim 58 \text{ mmol kg}^{-1}$ ) and adsorption rate ( $\sim 38 \mu\text{mol kg}^{-1} \text{s}^{-1}$ ) remained unchanged across all stacks. In addition, the coulomb efficiency ( $\sim 97\%$ ), specific capacitance ( $\sim 77 \text{ F g}^{-1}$ ), and electron efficiency ( $\sim 0.14$  molecular  $\text{CO}_2$   $\text{electron}^{-1}$ ) were consistent across all stacks as shown in Figure 13.

## 2.6. Sacrificial scrap metal-carbon dual electrode

The SSA effect can be employed to capture and sequester  $\text{CO}_2$  using a dual-material anode (Figure 14), consisting of a porous carbon component that acts as a capacitive  $\text{CO}_2$  concentrator and a sacrificial scrap metal (aluminum or steel) that functions

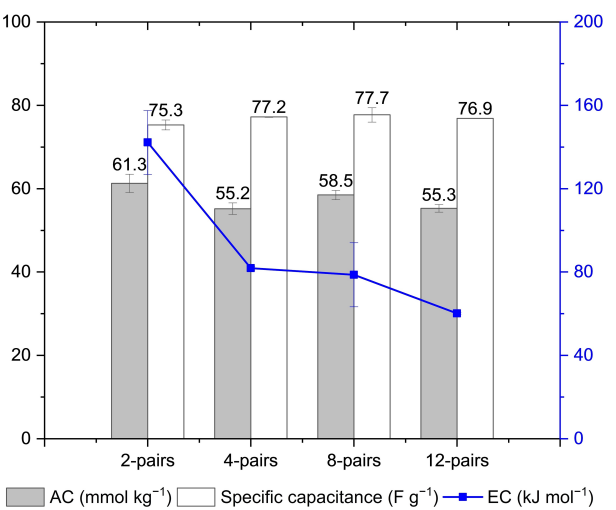


**Figure 13.** Performance metrics of tested SSA bipolar stacks. Reproduced from Ref. [73] Copyright (2023), with permission from ChemRxiv.

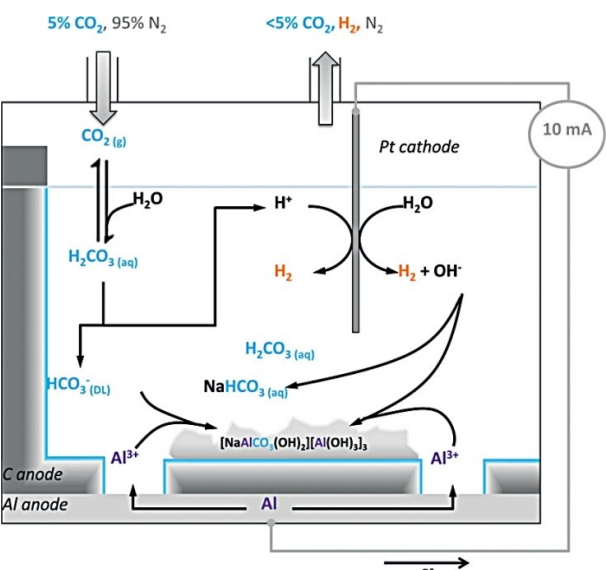


**Figure 14.** Electrochemical processes that drive carbon dioxide sequestration and mineralization in the aluminum-graphite anode cell. The formation of an electric double-layer is indicated by blue edges. Reproduced from Ref. [75] Copyright (2023), with permission from Wiley-VCH.

as a  $\text{CO}_2$  mineralizer, which appears to be a safer way to store  $\text{CO}_2$  compared to storing  $\text{CO}_2$  gas in empty oil and gas fields or on the seafloor.<sup>[74]</sup> On one hand, the anode capacitively adsorbs  $\text{CO}_2$ , leading to an enrichment of the concentration near the anode; on the other hand, the sacrificial metal component of the anode undergoes electrochemical oxidation, which results in the formation of an insoluble carbonaceous precipitate. At the cathode (e.g., Pt, Ni, or Fe electrode),  $\text{H}_2$  is released. Moreover, due to the  $\text{OH}^-$  ions produced at the cathode,  $\text{CO}_2$  gets sequestered as  $\text{NaHCO}_3$  in solution.

### 3. Perspectives

**Understanding of supercapacitive swing adsorption (SSA) mechanism.** Currently, the mechanism is based on hypotheses and reasoning, with only a limited number of experimental studies conducted. Previous research has demonstrated that approximately 20% of the pore volume of BPL carbon is infiltrated at uncharged chemical equilibrium, which provides a starting point for quantitative analysis of these mechanisms. However, the pore volume infiltration of BPL carbon during charging and discharging and after multiple charging and discharging remains to be explored. In addition, there is no guarantee that the pore volume infiltration of other activated carbons is consistent with BPL carbon, so the pore volume infiltration of various activated carbons at uncharged chemical equilibrium should be further explored. In conclusion, future exploration will focus on these mechanisms to gain a deeper understanding of SSA effect.

**Improvement of SSA performances.** Currently, it is worth exploring how to improve the CO<sub>2</sub> adsorption performance of SSA modules while maintaining cost-effectiveness. A breakthrough in this area could lead to the replacement of the conventional amine-washing method with supercapacitive swing adsorption of CO<sub>2</sub>. This review has presented various capacitive performances of different electrode materials (Figure 15), assuming that materials with high specific capacitance can achieve high CO<sub>2</sub> adsorption capacity, although further experimentation is required to confirm this hypothesis. More-

over, the effect of CO<sub>2</sub> and other gases (excluding N<sub>2</sub>) on the performance of SSA module has not been thoroughly studied. For instance, the separation of CO<sub>2</sub> from CH<sub>4</sub> gas to purify dry distillate gas could be a valuable area of research.

**Integration of SSA modules.** While supercapacitive swing adsorption of carbon dioxide has been studied in the laboratory, it has not yet been implemented in large-scale factories. However, researchers have made progress in scaling SSA modules by connecting electrode pairs in series, which has yielded positive performance feedback. In the future, further exploration of both series and parallel connections of SSA modules could lead to integrated systems with improved performances. Integrating SSA modules has become a promising research direction, as it is crucial in advancing SSA modules from the laboratory to industrial production.

### Acknowledgements

This work was financially supported by the National Natural Science Foundation of China (Nos. 52077207, 51907193, 52107234 and 52207250), Youth Innovation Promotion Association, CAS (No. Y2021052).

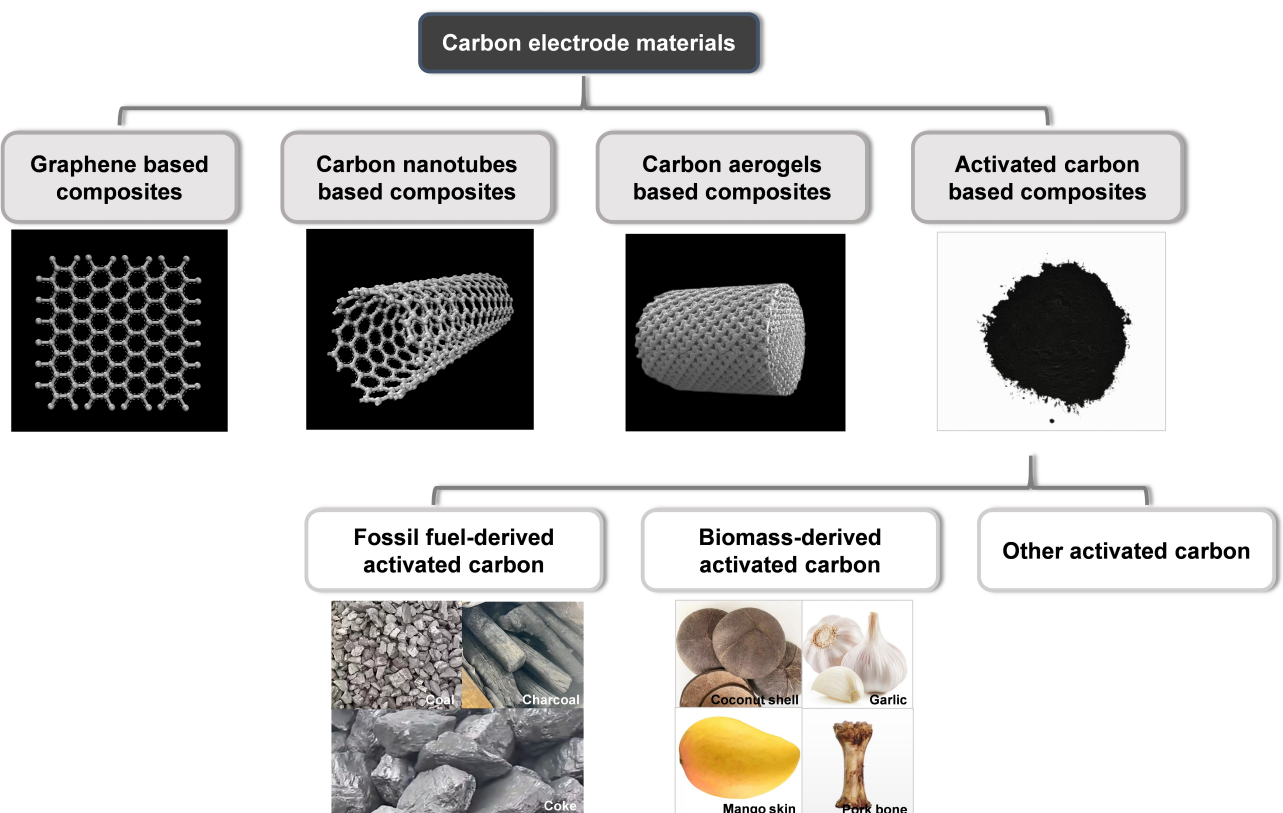


Figure 15. Different carbon electrode materials.

## Conflict of Interests

The authors declare that they have no known competing financial interests or personal relationships that could have appeared to influence the work reported in this paper.

## Data Availability Statement

The data that support the findings of this study are available from the corresponding author upon reasonable request.

**Keywords:** carbon dioxide capture • supercapacitive swing adsorption • capacitive materials • working mechanisms • structural design • influencing factors

- [1] a) N. James, M. Menzies, *Physica A* **2022**, *608*, 128302; b) N. Norahim, P. Yaisanga, K. Faungnawakij, T. Charinpanitkul, C. Klaysom, *Chem. Eng. Technol.* **2018**, *41*, 211–223.
- [2] a) Z. Sun, Z. Ma, M. Ma, W. Cai, X. Xiang, S. Zhang, M. Chen, L. Chen, *Buildings* **2022**, *12*, 128; b) L. Feng, D. Chen, S. Gao, Y. Wang, C. Tang, *J. Resour. Ecol.* **2019**, *10*, 94–103; c) Q. Guo, X. Xi, S. Yang, M. Cai, *Int. J. Miner., Metall. Mater.* **2022**, *29*, 626–634; d) P. Yang, S. Peng, N. Benani, L. Dong, X. Li, R. Liu, G. Mao, *J. Cleaner Prod.* **2022**, *377*, 134497.
- [3] a) M. Bui, C. S. Adjiman, A. Bardow, E. J. Anthony, A. Boston, S. Brown, P. S. Fennell, S. Fuss, A. Galindo, L. A. Hackett, J. P. Hallett, H. J. Herzog, G. Jackson, J. Kemper, S. Krevor, G. C. Maitland, M. Matuszewski, I. S. Metcalfe, C. Petit, G. Puxty, J. Reimer, D. M. Reiner, E. S. Rubin, S. A. Scott, N. Shah, B. Smit, J. P. M. Trusler, P. Webley, J. Wilcox, N. Mac Dowell, *Energy Environ. Sci.* **2018**, *11*, 1062–1176; b) G. T. Rochelle, *Science* **2009**, *325*, 1652–1654; c) C.-H. Yu, C.-H. Huang, C.-S. Tan, *Aerosol Air Qual. Res.* **2012**, *12*, 745–769; d) F. Meng, Y. Meng, T. Ju, S. Han, L. Lin, J. Jiang, *Renewable Sustainable Energy Rev.* **2022**, *168*, 112902.
- [4] a) H. Lin, J. Lu, A. M. Abed, K. Nag, M. Fayed, A. Deifalla, A. S. Bin Mahfouz, A. M. Galal, *Chemosphere* **2023**, *329*, 138583; b) N. S. Raghavan, M. M. Hassan, D. M. Ruthven, *AIChE J.* **1985**, *31*, 385–392; c) M. M. Hassan, N. S. Raghavan, D. M. Ruthven, H. A. Boniface, *AIChE J.* **1985**, *31*, 2008–2016; d) N. S. Raghavan, D. M. Ruthven, *AIChE J.* **1985**, *31*, 2017–2025; e) C. A. Grande, *ISRN Chem. Eng.* **2012**, *2012*, 982934; f) R. Krishna, *Microporous Mesoporous Mater.* **2012**, *156*, 217–223.
- [5] Y. Shen, Z. Niu, R. Zhang, D. Zhang, *J. CO<sub>2</sub> Util.* **2021**, *54*, 101764.
- [6] a) K. Wu, S. Deng, S. Li, R. Zhao, X. Yuan, L. Zhao, *Carbon Capture Sci. Technol.* **2022**, *2*, 100035; b) M. Clausse, J. Bonjour, F. Meunier, *Chem. Eng. Sci.* **2004**, *59*, 3657–3670.
- [7] L. Legrand, O. Schaetzel, R. C. F. de Kler, H. V. M. Hamelers, *Environ. Sci. Technol.* **2018**, *52*, 9478–9485.
- [8] J.-R. Li, R. J. Kuppler, H.-C. Zhou, *Chem. Soc. Rev.* **2009**, *38*, 1477–1504.
- [9] a) R. M. Siqueira, G. R. Freitas, H. R. Peixoto, J. F. d. Nascimento, A. P. S. Musse, A. E. B. Torres, D. C. S. Azevedo, M. Bastos-Neto, *Energy Procedia* **2017**, *114*, 2182–2192; b) Z. Liu, P. Hao, S. Li, X. Zhu, Y. Shi, N. Cai, *Adsorption* **2020**, *26*, 1239–1252.
- [10] X.-Y. Xin, J. Ma, H.-Q. Liu, Y.-J. Gu, Y.-F. Wang, H.-Z. Cui, *J. Mater. Sci. Technol.* **2023**, *151*, 66–72.
- [11] a) D. P. Chatterjee, A. K. Nandi, *J. Mater. Chem. A* **2021**, *9*, 15880–15918; b) B. Yang, D. Ruan, Y. Zhang, C. Wang, Z. Qiao, *Trans. Tianjin Univ.* **2020**, *26*, 391–398.
- [12] Y. Liu, S. P. Jiang, Z. Shao, *Mater. Today* **2020**, *7*, 100072.
- [13] B. Kokoszka, N. K. Jarrah, C. Liu, D. T. Moore, K. Landskron, *Angew. Chem. Int. Ed.* **2014**, *53*, 3698–3701.
- [14] a) R. Ben-Mansour, M. A. Habib, O. E. Bamidele, M. Basha, N. A. A. Qasem, A. Peedikakkal, T. Laoui, M. Ali, *Appl. Energy* **2016**, *161*, 225–255; b) A. A. Abd, S. Z. Naji, A. S. Hashim, M. R. Othman, *J. Environ. Chem. Eng.* **2020**, *8*, 104142.
- [15] a) L. Riboldi, O. Bolland, *Energy Procedia* **2017**, *114*, 2390–2400; b) T. T. T. Nguyen, G. K. H. Shimizu, A. Rajendran, *Chem. Eng. J.* **2023**, *452*, 139550; c) B. J. Maring, P. A. Webley, *Int. J. Greenhouse Gas Control* **2013**, *15*, 16–31.
- [16] R. Zhao, L. Liu, L. Zhao, S. Deng, S. Li, Y. Zhang, *Renewable Sustainable Energy Rev.* **2019**, *114*, 109285.
- [17] S. Zhu, K. Ma, K. Landskron, *J. Phys. Chem. C* **2018**, *122*, 18476–18483.
- [18] Y. Liu, C. Li, C. Liu, Y. Chen, K. An, K. Landskron, *Carbon* **2018**, *136*, 139–142.
- [19] S. Zhu, J. Li, A. Toth, K. Landskron, *ACS Appl. Energ. Mater.* **2019**, *2*, 7449–7456.
- [20] T. B. Binford, G. Mapstone, I. Temprano, A. C. Forse, *Nanoscale* **2022**, *14*, 7980–7984.
- [21] S. Zhu, J. Li, A. Toth, K. Landskron, *ACS Appl. Mater. Interfaces* **2019**, *11*, 21489–21495.
- [22] C. Liu, K. Landskron, *Chem. Commun.* **2017**, *53*, 3661–3664.
- [23] M. Bilal, J. Li, K. Landskron, *ChemRxiv preprint* **2022** DOI: 10.26434/chemrxiv-2022-26fb5v2.
- [24] a) M. Bora, J. Tamuly, S. M. Benoy, S. Hazarika, D. Bhattacharja, B. K. Saikia, *Fuel* **2022**, *329*, 125385; b) G. Song, C. Romero, T. Lowe, G. Driscoll, B. Kreglow, H. Schobert, J. Baltrusaitis, Z. Yao, *Energy Fuels* **2023**, *37*, 1327–1343; c) L. Wang, F. Sun, J. Gao, X. Pi, T. Pei, Z. Qie, G. Zhao, Y. Qin, *J. Taiwan Inst. Chem. Eng.* **2018**, *91*, 588–596.
- [25] a) M. Kim, J. Kim, *Phys. Chem. Chem. Phys.* **2014**, *16*, 11323–11336; b) R. Venkatkarthick, J. Qin, T. Maiyalagan, *Int. J. Energy Res.* **2022**, *46*, 22474–22485.
- [26] a) R. Priyadarshini, R. Saravanathamizhan, V. Manimozhi, J. Manokaran, N. Balasubramanian, *Energ. Storage* **2020**, *61*, e151; b) Y. Zhang, T. Cai, J. Huang, W. Xing, Z. Yan, *J. Mater. Res.* **2016**, *31*, 3723–3730.
- [27] a) R. S. Jeniffer, V. Raghavan, *J. Electrochem. Sci. Eng.* **2022**, *12*(3), 54; b) J. Devarajan, P. Arumugam, *J. Mater. Sci. Mater. Electron.* **2022**, *33*, 17469–17482; c) X. Z. Sun, X. Zhang, H. T. Zhang, D. C. Zhang, Y. W. Ma, *J. Solid State Electrochem.* **2012**, *16*, 2597–2603; d) X. Z. Sun, X. Zhang, D. C. Zhang, Y. W. Ma, *Acta Phys. Chim. Sin.* **2012**, *28*, 367–372; e) K. Wang, X. Zhang, C. Li, X. Sun, Q. Meng, Y. Ma, Z. Wei, *Adv. Mater.* **2015**, *27*, 7451–7457; f) X. Zhang, X. Z. Sun, H. T. Zhang, C. Li, Y. W. Ma, *Electrochim. Acta* **2014**, *132*, 315–322; g) X. Zhang, X. Z. Sun, H. T. Zhang, D. C. Zhang, Y. W. Ma, *Mater. Chem. Phys.* **2012**, *137*, 290–296.
- [28] a) Y. Jiang, J. Li, Z. Jiang, M. Shi, R. Sheng, Z. Liu, S. Zhang, Y. Cao, T. Wei, Z. Fan, *Carbon* **2021**, *175*, 281–288; b) Z. Wang, M. Zhu, Z. Pei, Q. Xue, H. Li, Y. Huang, C. Zhi, *Mater. Sci. Eng. R* **2020**, *139*, 100520; c) M. Maher, S. Hassan, K. Shoueir, B. Yousif, M. E. A. Abo-Elsoud, *J. Mater. Res. Technol.* **2021**, *11*, 1232–1244.
- [29] S. Saini, P. Chand, A. Joshi, *J. Energy Storage* **2021**, *39*, 102646.
- [30] a) P. Merin, P. Jimmy Joy, M. N. Muralidharan, E. Veena Gopalan, A. Seema, *Chem. Eng. Technol.* **2021**, *44*, 844–851; b) J. Deng, M. Li, Y. Wang, *Green Chem.* **2016**, *18*, 4824–4854.
- [31] Y. Gao, L. Li, Y. Jin, Y. Wang, C. Yuan, Y. Wei, G. Chen, J. Ge, H. Lu, *Appl. Energy* **2015**, *153*, 41–47.
- [32] K. Subramani, N. Sudhan, M. Karnan, M. Sathish, *ChemistrySelect* **2017**, *2*, 11384–11392.
- [33] J. Liu, H. Li, H. Zhang, Q. Liu, R. Li, B. Li, J. Wang, *J. Solid State Chem.* **2018**, *257*, 64–71.
- [34] Z. Xiao, *Int. J. Electrochem. Sci.* **2018**, 5370–5381.
- [35] A. A. Mohammed, C. Chen, Z. Zhu, *J. Colloid Interface Sci.* **2019**, *538*, 308–319.
- [36] Q. Xie, R. Bao, A. Zheng, Y. Zhang, S. Wu, C. Xie, P. Zhao, *ACS Sustainable Chem. Eng.* **2016**, *4*, 1422–1430.
- [37] Q. Yuan, Z. Ma, J. Chen, Z. Huang, Z. Fang, P. Zhang, Z. Lin, J. Cui, *Polymer* **2020**, *12*, 1982.
- [38] T. E. Rufford, D. Hulicova-Jurcakova, Z. Zhu, G. Q. Lu, *Electrochim. Commun.* **2008**, *10*, 1594–1597.
- [39] F. Jerez, P. B. Ramos, V. E. Córdoba, M. F. Ponce, G. G. Acosta, M. A. Bavia, *J. Environ. Manage.* **2023**, *330*, 117158.
- [40] C. Peng, X.-b. Yan, R.-t. Wang, J.-w. Lang, Y.-j. Ou, Q.-j. Xue, *Electrochim. Acta* **2013**, *87*, 401–408.
- [41] Y. Wang, C. Shao, S. Qiu, Y. Zhu, M. Qin, Y. Meng, Y. Wang, H. Chu, Y. Zou, C. Xiang, J.-L. Zeng, Z. Cao, F. Xu, L. Sun, *Diamond Relat. Mater.* **2019**, *98*, 107475.
- [42] M. Karnan, K. Subramani, N. Sudhan, N. Ilayaraja, M. Sathish, *ACS Appl. Mater. Interfaces* **2016**, *8*, 35191–35202.
- [43] X. Kong, Y. Zhang, P. Zhang, X. Song, H. Xu, *Appl. Surf. Sci.* **2020**, *516*, 146162.
- [44] D. J. Tarimo, K. O. Oyedotun, N. F. Sylla, A. A. Mirghani, N. M. Ndiaye, N. Manyala, *J. Energy Storage* **2022**, *51*, 104378.
- [45] V. Yang, R. A. Senthil, J. Pan, A. Khan, S. Osman, L. Wang, W. Jiang, Y. Sun, *J. Electroanal. Chem.* **2019**, *855*, 113616.
- [46] T. Jin, J. Su, Q. Luo, W. Zhu, H. Lai, D. Huang, C. Wang, *ACS Omega* **2022**, *7*, 37564–37571.
- [47] J. Phiri, J. Dou, T. Vuorinen, P. A. C. Gane, T. C. Maloney, *ACS Omega* **2019**, *4*, 18108–18117.

- [48] R. M. Bhattacharai, K. Chhetri, S. Natarajan, S. Saud, S. J. Kim, Y. S. Mok, *Chemosphere* **2022**, *303*, 135290.
- [49] L. K. Shrestha, R. G. Shrestha, R. Chaudhary, R. R. Pradhananga, B. M. Tamrakar, T. Shrestha, S. Maji, R. L. Shrestha, K. Ariga, *Nanomaterials* **2021**, *11*, 3175.
- [50] J. Zhou, L. Bao, S. Wu, W. Yang, H. Wang, *Carbohydr. Polym.* **2017**, *173*, 321–329.
- [51] J. P. Paraknowitsch, A. Thomas, *Energy Environ. Sci.* **2013**, *6*, 2839–2855.
- [52] H. Qu, X. Zhang, J. Zhan, W. Sun, Z. Si, H. Chen, *ACS Sustainable Chem. Eng.* **2018**, *6*, 7380–7389.
- [53] P. R. Varadwaj, A. Varadwaj, H. M. Marques, K. Yamashita, *Compounds* **2022**, *2*, 80–110.
- [54] a) X. Zhao, C. Li, X. Zhang, X. Sun, K. Wang, X. Huang, Y. Ma, *ChemistrySelect* **2017**, *2*, 6194–6199; b) C. Li, X. Zhang, K. Wang, X. Sun, Y. Xu, F. Su, C.-M. Chen, F. Liu, Z.-S. Wu, Y. Ma, *NPG Asia Mater.* **2021**, *13*, 59; c) D. Dong, Y. Zhang, Y. Xiao, T. Wang, J. Wang, C. E. Romero, W.-p. Pan, *J. Colloid Interface Sci.* **2020**, *580*, 77–87; d) Q. Lv, W. Si, J. He, L. Sun, C. Zhang, N. Wang, Z. Yang, X. Li, X. Wang, W. Deng, Y. Long, C. Huang, Y. Li, *Nat. Commun.* **2018**, *9*, 3376.
- [55] C. Sun, X. Zhang, C. Li, K. Wang, X. Sun, Y. Ma, *Energy Storage Mater.* **2020**, *32*, 497–516.
- [56] a) L. R. Radovic, M. Karra, K. Skokova, P. A. Thrower, *Carbon* **1998**, *36*, 1841–1854; b) S. Bubin, L. Adamowicz, *Phys. Rev. Lett.* **2017**, *118*, 043001.
- [57] H. Sun, M. Wang, X. Du, Y. Jiao, S. Liu, T. Qian, Y. Yan, C. Liu, M. Liao, Q. Zhang, L. Meng, L. Gu, J. Xiong, C. Yan, *J. Mater. Chem. A* **2019**, *7*, 20952–20957.
- [58] W. Lei, J. Guo, Z. Wu, C. Xuan, W. Xiao, D. Wang, *Sci. Bull.* **2017**, *62*, 1011–1017.
- [59] Z. Q. He, D. D. Chen, M. Wang, C. X. Li, X. Y. Chen, Z. J. Zhang, *J. Electroanal. Chem.* **2020**, *856*, 113678.
- [60] X. Long, Z. Li, G. Gao, P. Sun, J. Wang, B. Zhang, J. Zhong, Z. Jiang, F. Li, *Nat. Commun.* **2020**, *11*, 4074.
- [61] X. Sun, J. Xu, Y. Ding, B. Zhang, Z. Feng, D. S. Su, *ChemSusChem* **2015**, *8*, 2872–2876.
- [62] L. Zhao, *RSC Adv.* **2017**, *7*, 13904–13910.
- [63] a) Y. Hernandez, V. Nicolosi, M. Lotya, F. M. Blighe, Z. Sun, S. De, I. T. McGovern, B. Holland, M. Byrne, Y. K. Gun'ko, J. J. Boland, P. Niraj, G. Duesberg, S. Krishnamurthy, R. Goodhue, J. Hutchison, V. Scardaci, A. C. Ferrari, J. N. Coleman, *Nat. Nanotechnol.* **2008**, *3*, 563–568; b) W. Liu, X. Zhang, Y. Xu, L. Wang, Z. Li, C. Li, K. Wang, X. Sun, Y. An, Z. S. Wu, *Adv. Funct. Mater.* **2022**, *32*, 2202342; c) Li, X. Zhang, K. Wang, H.-t. Zhang, X.-z. Sun, Y.-w. Ma, *Carbon* **2015**, *93*, 1085; d) V. B. Mbayachi, E. Ndayiragije, T. Sammani, S. Taj, E. R. Mbuta, A. U. Khan, *Results Chem.* **2021**, *3*, 100163; e) J. Wang, F. Ma, M. Sun, *RSC Adv.* **2017**, *7*, 16801–16822; f) Y. Chen, X. Zhang, H. T. Zhang, X. Z. Sun, D. C. Zhang, Y. W. Ma, *RSC Adv.* **2012**, *2*, 7747–7753; g) X. Zhang, H. Zhang, C. Li, K. Wang, X. Sun, Y. Ma, *RSC Adv.* **2014**, *4*, 45862–45884; h) W. Lv, D.-M. Tang, Y.-B. He, C.-H. You, Z.-Q. Shi, X.-C. Chen, C.-M. Chen, P.-X. Hou, C. Liu, Q.-H. Yang, *ACS Nano* **2009**, *3*, 3730–3736.
- [64] L. Liu, R. Zhang, Y. Liu, H. Zhu, W. Tan, G. Zhu, Y. Wang, *Trans. Tianjin Univ.* **2018**, *24*, 555–562.
- [65] Z. Zhang, K. Chi, F. Xiao, S. Wang, *J. Mater. Chem. A* **2015**, *3*, 12828–12835.
- [66] M. D. Stoller, S. Park, Y. Zhu, J. An, R. S. Ruoff, *Nano Lett.* **2008**, *8*, 3498–3502.
- [67] a) E. T. Thostenson, Z. Ren, T.-W. Chou, *Compos. Sci. Technol.* **2001**, *61*, 1899–1912; b) S. Rathinavel, K. Priyadarshini, D. Panda, *Mater. Sci. Eng. B* **2021**, *268*, 115095; c) R. Dubey, D. Dutta, A. Sarkar, P. Chattopadhyay, *Nanoscale Adv.* **2021**, *3*, 5722–5744; d) M. N. S. K. V. P. S. M. S. R. G. V. S. K. S. T. K., *Mater. Today: Proc.* **2021**, *47*, 4682–4685.
- [68] V. Subramanian, H. Zhu, B. Wei, *Electrochem. Commun.* **2006**, *8*, 827–832.
- [69] H. Peçenek, F. K. Dokan, M. S. Onses, E. Yilmaz, E. Sahmetlioglu, *Mater. Res. Bull.* **2022**, *149*, 111745.
- [70] a) H. Liu, T. Xu, C. Cai, K. Liu, W. Liu, M. Zhang, H. Du, C. Si, K. Zhang, *Adv. Energy Mater.* **2022**, *32*, 2113082; b) J.-H. Lee, S.-J. Park, *Carbon* **2020**, *163*, 1–18; c) N. Liu, J. Shen, D. Liu, *Microporous Mesoporous Mater.* **2013**, *167*, 176–181; d) J. Zeng, Z. Chen, M. Li, Y. Guo, J. Xu, X. Zhao, H. Lu, *Chem. Mater.* **2022**, *34*, 9172–9181.
- [71] a) Y. Xu, S. Wang, B. Ren, J. Zhao, L. Zhang, X. Dong, Z. Liu, *J. Colloid Interface Sci.* **2019**, *537*, 486–495; b) F. Lai, Y. E. Miao, L. Zuo, H. Lu, Y. Huang, T. Liu, *Small* **2016**, *12*, 3235–3244.
- [72] M. Bilal, J. Li, H. Guo, K. Landskron, *Small* **2023**, *19*, 2207834.
- [73] J. Li, M. Bilal, K. Landskron, *ChemRxiv preprint* **2023**, DOI: 10.26434/chemrxiv-2023-62xjd.
- [74] K. Landskron, *Angew. Chem. Int. Ed.* **2018**, *57*, 3548–3550.
- [75] K. J. Lamb, M. R. Dowsett, K. Chatzipanagis, Z. W. Scullion, R. Kröger, J. D. Lee, P. M. Aguiar, M. North, A. Parkin, *ChemSusChem* **2018**, *11*, 137–148.

Manuscript received: July 4, 2023

Revised manuscript received: September 12, 2023

Accepted manuscript online: September 12, 2023

Version of record online: September 28, 2023